Available online at www.sciencedirect.com
ScienceDirect
Solid-State Electronics xxx (2006) xxx–xxx
SOLID-STATE ELECTRONICS
www.elsevier.com/locate/sse

Electroabsorption modulator performance predicted from band-edge absorption spectra of bulk, quantum-well, and quantum-well-intermixed InGaAsP structures

Gordon B. Morrison [a,*], James W. Raring [c], Chad S. Wang [b], Erik J. Skogen [c], Yu-Chia Chang [b], Matt Sysak [b], L.A. Coldren [b]

[a] *Apogee Photonics, 6580 Snow Drift Road, Suit 100, Allentown, PA 18106, USA*
[b] *Department of Electrical and Computer Engineering, University of California, Santa Barbara, CA 93106, USA*
[c] *Sandia National Labs, Albuquerque, NM, 87123, USA*

Received 20 December 2005; accepted 26 October 2006

The review of this paper was arranged by Prof. Y. Arakawa

Abstract

Band-edge absorption spectra from bulk, quantum-well, and quantum-well-intermixed InGaAsP material are collected and compared using photocurrent spectroscopy. The expected performances of ideal electroabsorption modulators fabricated from these materials are predicted and compared using the band-edge absorption data. A graphical method for simultaneously considering chirp, insertion-loss, extinction-ratio, and tuning range is presented, and is used to compare the suitability of the various materials for electroabsorption modulator applications. The quantum-well material is shown to be superior to bulk material for most EAM applications. Quantum wells with 85 meV conduction band depth and 80 Å width are shown to be superior to quantum wells with 120 meV conduction band depth and 65 Å width. Both well designs exhibit strong excitons. Finally, the effect of quantum-well intermixing is considered, and the expected performances of quantum-well-intermixed electroabsorption modulators are presented.

Keywords: Photocurrent spectroscopy; Electroabsorption; Modulator; Quantum confined Stark effect; Franz–Keldysh effect; Chirp; Exciton; Bandwidth; Quantum well; Bulk material; Tunable

1. Introduction

Electroabsorption modulators (EAM) are key components in modern fiber-optic communication systems. Discrete EAMs can be co-packaged with lasers to form integrated transmitter modules, but EAMs monolithically integrated with semiconductor lasers are now commercially available at both 1550 nm and 1310 nm. A wide variety of methods have been used for monolithic integration of lasers with EAMs on InP, including asymmetric twin waveguides (ATG) [1,2], quantum well intermixing (QWI) [3,4], identical active layers [5], offset quantum wells [6], dual quantum wells [7,8], butt-coupling regrowth [9,10] and selective area regrowth (SAG) [11]. With growing demand for bandwidth, increasingly complex photonic integrated circuits (PICs) that include EAMs are under development [6].

Regardless of the integration platform, the optimal performance of the modulator is ultimately limited by the band-edge absorption characteristics of the material from which it is fabricated. Therefore, a comprehensive knowledge of the band-edge absorption characteristics of various

* Corresponding author. Tel.: +1 610 706-0282.
E-mail address: gordon.morrison@apogeephotonics.com (G.B. Morrison).

0038-1101/$ - see front matter © 2006 Elsevier Ltd. All rights reserved.
doi:10.1016/j.sse.2006.10.013

EAM materials is mandatory. Insights into the relationship between band-edge absorption spectra and EAM performance are also vital for optimal EAM design.

The fundamental property requisite in an EAM material is that an applied bias will change the band-edge absorption spectrum. This property can be induced in InGaAsP by two distinct mechanisms. One of these mechanisms is the Franz–Keldysh effect, and occurs in bulk material. An electric field is applied to the bulk material so that the electron and valence energy bands are tilted. The carrier wavefunctions can tunnel into the tilted bands so that lower energy photons can excite an electron into the conduction band [12]. Thus, under a reverse bias, the absorption spectrum of the bulk material shifts to longer wavelengths. The electroabsorption coefficient of this Franz–Keldysh mechanism can be approximated for weak fields using Airy functions [13]. The other mechanism commonly used for InP EAM modulators is the quantum confined Stark effect (QCSE), which occurs in quantum well structures. Carriers are confined to the quantum wells, and the electron–hole pairs form excitons at room temperature, even in the presence of electric fields. The exciton binding energy manifests itself in the QW band-edge absorption spectrum as an absorption-peak (exciton peak). When an electric field is applied, the conduction and valence bands are tilted, altering the shape of the potential well. The altered well potential results in a reduced overlap of electron and hole wavefunctions, and the magnitude of the exciton peak is reduced. The energy levels of the electron and hole are also reduced, and lower energy photons can be absorbed [14]. Therefore, under a reverse bias, the absorption spectrum of the QW structure shifts to longer wavelengths.

In this work, the band-edge absorption spectra of bulk, quantum-well (QW), and QWI InGaAsP materials grown on InP are obtained by a photocurrent spectroscopy technique [15–19]. The band-edge absorption characteristics of these structures are compared and contrasted, and are related to the predicted performances of ideal EAMs fabricated from similar epitaxial structures. An ideal EAM is assumed to operate without undesirable second order effects such as saturation, or heating. Photocurrent spectroscopy data does not yield insight into the effects of heating or saturation because the photodiodes are characterized using very low light intensity. The photocurrent is less than 1 μA, and neither heating nor saturation is present. In general, small amounts of heating are expected to red-shift the modulator band-edge. Saturation is undesirable in EAMs because the build up of carriers reduces both extinction and RF performance. A well-designed EAM should be free from saturation in its operating regime (carriers are easily swept out of the active region by the electic field), and therefore predictions made from band-edge absorption data are expected to be accurate.

The validity of using photocurrent spectroscopy data to predict modulator characteristics such as extinction and chirp has been demonstrated previously [18,19]. Kim et. al. have also demonstrated the use of electroabsorption spectroscopy for accurate prediction of various modulator characteristics [20].

To correctly describe EAM performance, many characteristics must be simultaneously examined. The insertion-loss of an EAM should be as low as possible to avoid optical power attenuation. The extinction-ratio should be large, to keep the bit-error-rate (BER) low, and to reduce power penalty. For many telecommunications applications, the large signal chirp should be low, or preferably negative, to compensate for the dispersive properties of the optical fiber. A large wavelength tuning range is also desirable for applications such as uncooled (i.e., wavelength variable) transmitters [21], or broadly tunable transmitters [22]. In this paper, we combine photocurrent spectroscopy predictions with novel graphical analysis to simultaneously consider EAM tuning range, chirp, extinction, and insertion-loss. A comprehensive comparison of the suitability of various different materials to EAM applications is thereby enabled. Although the data presented in this paper are for a finite number of epitaxial structures, the results and trends from these structures offer insights into a wider range of possible designs.

2. Experiment

2.1. Photocurrent spectroscopy

In this work we employ a Varian Cary 500 spectrophotometer as the wavelength-tunable light source. The Cary 500 has a wide UV/Vis/NIR bandwidth ranging from 175 nm to 3000 nm. The photodiode is connected to a Keithly 2400 L–V source meter that scans across a range of reverse biases. A 3 kHz chopper samples the spectrophotometer optical source and an EG&G 5210 lock-in amplifier is used to reject leakage current and other noise. A 1 mm diameter aperture samples light from the spectrophotometer beam, and input light is calibrated using a Newport1835 C optical power meter. The entire system is automated. A basic diagram of the apparatus is shown in Fig. 1.

The photocurrent data is converted to a measure of electrons per second or equivalently the number of photons absorbed per second. The incident optical power is known,

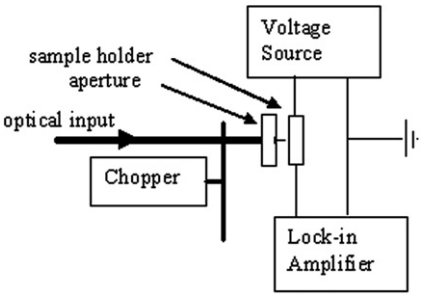

Fig. 1. Block diagram of the photocurrent spectroscopy test bench.

Please cite this article in press as: Morrison GB et al., Electroabsorption modulator performance predicted ..., Solid State Electron (2006), doi:10.1016/j.sse.2006.10.013

and is scaled down appropriately to account for absorption in the contact layer and reflection from the air/semiconductor surface. Weak optical interference between the contact layer and underlying semiconductor was noted during transmission and reflection measurements using the Cary 500 spectrophotometer, and these weak interference effects were taken into consideration during calibration of the optical input. Calculation of absorption is performed using

$$\alpha_{abs} = -\ln\left(\frac{P_{in} - P_c}{P_{in}}\right)\Big/ L \quad (1)$$

where α_{abs} is the power absorption per unit length of material, P_{in} is the number of photons entering the photodiode per second, P_c is the number of photons per second absorbed and measured as photocurrent, and L is the length of the absorbing material.

2.2. Epitaxial structures

The band-edge absorption spectra of three distinct epitaxy layer structures are considered in this paper. Each structure contains a slab-waveguide suitable for fabrication of ridge-waveguide components. The first structure employs a 3500 Å (i.e., bulk) InGaAsP absorbing layer with a band-edge of 1.395 μm (1.395Q). Due to the thick nature of the absorbing material, this structure exhibits the Franz–Keldysh effect, and is therefore useful for EAM applications.

The second structure considered in this paper consists of 15 compressively strained 80 Å wells and 16, 80 Å barriers centered in a 1.1Q waveguide. The conduction band depth in the wells is approximately 85 meV. These wells exhibit a photoluminescence peak (λ-PL) of 1554 nm. There are 650 Å of unintentionally doped material on either side of the wells. Quantum well structures exhibit the Quantum Confined Stark Effect and are therefore useful for EAM applications.

The final distinct structure contains 10 compressively strained 65 Å wells and 11, 80 Å barriers all centered within a 1.3Q waveguide. The conduction band depth in these wells is approximately 120 meV. These wells exhibit a λ-PL of 1556 nm. There are 1050 Å of unintentionally doped material on either side of these wells. The net width of unintentionally doped material in each QW structure is similar, thus the two structures exhibit similar electric fields across their wells.

Each of the QW structures has been subjected to various degrees of QWI. The characteristics of these QWI structures are also considered in this paper.

2.3. Photodiode fabrication

Prior to the fabrication process, parts of the QW samples are blue-shifted by QWI. Initially, each structure consists of the waveguide beneath a 15 nm InP layer, 20 nm 1.3Q etch stop, and a 450 nm InP implant buffer layer. A 5000 Å SixNy mask layer is deposited on the samples, and is selectively removed to define areas for QWI. A 100 keV, 5e14 cm-2 dose of P+ is implanted into the buffer layer. Regions protected by the 5000 Å of SixNy remain implant-free, and therefore do not experience QWI. Rapid thermal annealing at 675 °C is performed to drive point defects from the implant buffer layer through the quantum wells [3]. The magnitude of the blue-shift is controlled by the anneal time. Multiple band-edges are obtained on a single sample by annealing to the desired blue-shift, selectively removing the ion implant buffer layer, and then further annealing the sample. Areas that have had the buffer layer removed remain at a fixed wavelength throughout subsequent annealing, whereas areas retaining the implant buffer layer are blue-shifted further.

The fabrication process for each material is identical. Circular photodiodes ranging from 50 μm to 400 μm in radius are patterned on each sample (the data presented in this paper were obtained using 250 μm photodiodes). A reactive-ion etch process is used to etch through the waveguide and active region of the material. A 2000 Å SixNy layer is deposited over the sample, and circular vias are etched into the SixNy to expose the mesa contact layers. Ti/Pt/Au ring contacts are deposited on top of the mesas. The photodiodes are designed for operation with very small (often less than 1 μA) photocurrent, therefore resistance caused by the ring contact does not constitute a significant voltage drop. Finally, the samples are thinned and back-side metalized. A 30 s contact anneal at 420 °C is performed to reduce ohmic resistance and avoid schottky barriers. The photodiodes are mounted and wire bonded on AlN carriers. The fabrication process for these absorption-edge spectroscopy photodiodes can be completed very rapidly with minimal effort, making absorption-edge spectroscopy a useful and realistic tool for assisting in the design of optimized photonic integrated circuits. Fig. 2 shows a side-view of a typical photodiode for photocurrent spectroscopy.

Some samples were grown on Fe-doped substrates rather than n-type substrates. For samples on Fe-doped substrates, vias are opened on the top side for the n-contacts. These Fe-doped samples do not require back-side

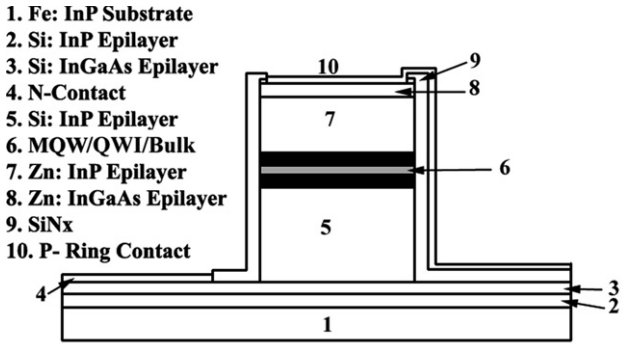

Fig. 2. Cross sectional view of a simple photodiode used for photocurrent spectroscopy.

metallization for the n-contact, and heating is not an issue with such very small photocurrents. Interestingly, samples without back-side metallization produce about 35% more photocurrent than their back-side metalized counterparts, and did not result in predictions consistent with modulators fabricated from the same material. Furthermore, back-side metal deposition reduces the photocurrent in previously unmetalized devices by 35%. The explanation for this phenomenon is that without back-side metallization, a fraction of light is scattered from the back-side of the sample and is able to pass through the absorbing region of the photodiode a second time. The back-side metallization and annealing process eliminates the back-scattering effect, and the subsequent photocurrent data has been shown to agree well with actual modulator performance [18,19].

2.4. Data and observations

Figs. 3–5 show the band-edge absorption spectra for bulk material, 80 Å wells, and 65 Å wells, respectively. In Figs. 4 and 5, the band-edge absorption spectra of the QWI materials are also presented. An exciton peak is clearly visible in QW structures. In contrast, there is no exciton peak in the bulk absorption-edge. The Stark shift in the 80 Å wells is much larger than that in the 65 Å wells, and the excitons in the 80 Å wells decay much faster than the excitons in the 65 Å wells. These simple observations are in excellent agreement with previous experiments and well-known absorption-edge theory [23].

The blue-shift associated with QWI occurs when group V atoms diffuse across the as-grown QW compositional boundaries, causing the QWs to develop rounded edges and become wider, shallower, and more parabolic. The exciton peaks in Figs. 4 and 5 decay more rapidly in the intermixed QWs than in the as-grown QWs. This weakening of the exciton is consistent with decreased carrier confinement in the intermixed wells.

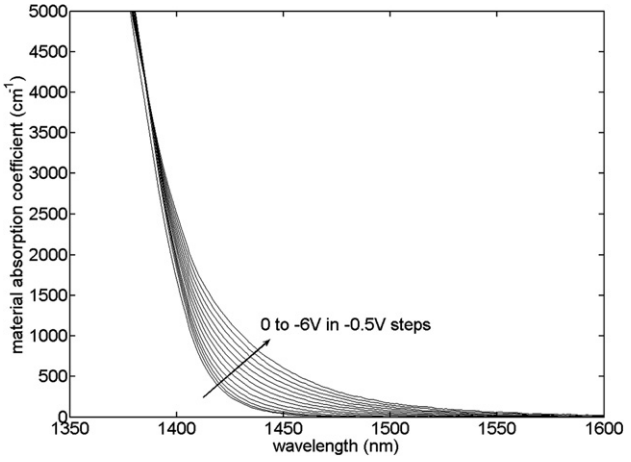

Fig. 3. Absorption-edge in bulk material. Data is shown ranging from 0 to −6 V in −0.5 V steps.

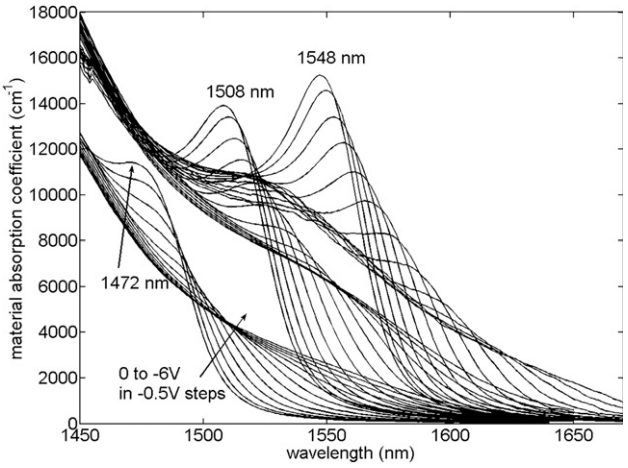

Fig. 4. Band-edge absorption spectra for the 80 Å QW structure at various applied biases. Also shown are the blue-shifted band-edge absorption spectra obtained from the same structure after different amounts of QWI. Each absorption-edge has been measured with biases ranging from 0 V to −6 V in −0.5 V steps.

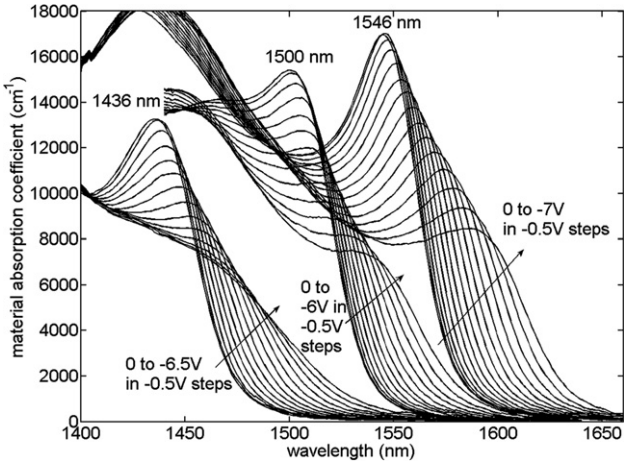

Fig. 5. Band-edge absorption spectra in the 65 Å quantum-well structure at various applied biases. Also shown are the blue-shifted band-edge absorption spectra obtained from the same structure after different amounts of QWI. Each absorption-edge is shown for a range of different bias voltages separated by 0.5 V steps.

The data in Figs. 4 and 5 provide a unique opportunity for simple observations comparing the effect of QWI on the band-edge absorption spectra of different QW structures. The maximum QWI blue-shift that was obtainable in the shallower 80 Å wells of Fig. 4 was only 70 nm, compared to the 108 nm shift of the narrower, deeper wells in Fig. 5. It is evident that the structure and eigenenergies of the deeper, narrower wells of Fig. 5 are more susceptible to QWI than the shallower, wider wells of Fig. 4. This difference in response to the intermixing process occurs for two reasons. First, the deeper wells have a larger compositional difference at the well boundary, which enhances diffusion of group V atoms between the well and the barrier, resulting in a larger perturbation to the well structure. Secondly, the diffusion process originates from the material

Please cite this article in press as: Morrison GB et al., Electroabsorption modulator performance predicted ..., Solid State Electron (2006), doi:10.1016/j.sse.2006.10.013

composition interface at the edges of the well, so that the diffusion process has greater influence throughout the narrow well. The center of the wider well is further from the material interface, and thus less susceptible to the diffusion process.

The optical loss in intermixed material has been shown previously [24] to depend exponentially on how far the material is intermixed from operation wavelength. This phenomenon is clearly observable in Figs. 4 and 5. The degree of absorption at 1550 nm for the passive (1436 nm) material in Fig. 5 will be less than the absorption of the passive (1472 nm) material in Fig. 4. Furthermore, the 0 V absorption for the deeper, narrower well approaches zero as a function of wavelength faster than the 0 V absorption of the wider, shallower well. Thus, from a passive material insertion-loss perspective, the deeper wells of Fig. 5 may have a significant advantage.

3. Analysis and results

3.1. Calculations

In this paper, scattering losses and other process-dependent insertion-losses are not included in the analysis. The insertion-loss considered in this paper is simply the loss due to absorption when the modulator is at its smallest bias (i.e., the optical power "on" state). The extinction is the ratio, in dB, between the "off" state and "on" state of the modulator. The chirp parameter measures the relationship between change in signal amplitude and change in carrier frequency. Low or negative chirp values are desirable as they are necessary to counter the dispersion inherent to optical fiber [25].

The absorption-edge data in Figs. 3–5, are easily manipulated to predict EAM extinction. The low input optical power used in the photocurrent spectroscopy experiments makes the predictions valid for optimally designed, ideal devices, in which second order effects such as heating, contact resistance, saturation and optical scattering are presumed negligible. The extinction (dB) as a function of wavelength and voltage is determined by

$$z = 10\log(e^{\alpha_{abs}\Gamma L_{eff}}) \tag{2}$$

where Γ is the overlap integral between the optical mode and the absorbing material, L is the effective length of the device, and α_{abs} is the material absorption, which is a function of wavelength and voltage. In previous work [18,20], DC extinction predictions have been shown to agree well with data from real EAM devices fabricated from the same material. Any wavelength-independent errors (e.g., scattering, measurement of optical input) in determination of α in Eq. (1) would simply mean that predictions from Eq. (2). are correct but for a slightly different modulator length. For example, a 10% overestimation of α_{abs} would mean that extinction predictions are actually for a modulator 10% shorter in length than the one considered. Similarly, errors in estimation of optical confinement (Γ) would result only in an inversely proportional error in the stated modulator length. The sum of measurement errors and errors in estimation of optical confinement are estimated to be less than 10%.

Starting with a change in absorption as a function of bias and wavelength, changes in index of refraction as a function of bias and wavelength are easily obtained using the Kramers–Kronig transform,

$$\Delta n(\lambda_0, \Delta V) = \frac{\lambda_0^2}{2\pi^2} P \int_0^\infty \frac{\Delta\alpha_{abs}(\lambda, \Delta V)}{\lambda_0^2 - \lambda^2} d\lambda \tag{3}$$

where Δn is the change in index of refraction at wavelength λ_0 due to a bias change ΔV, and P indicates the principle value of the integral. Of course, Eq. (2). is also a function of V_0, the bias point at which ΔV is centered. The singularity at $\lambda = \lambda_0$ is avoided using the transformation described by Henry et al. in [26]. Note that the denominator in the Kramers–Kronig transform acts somewhat as a filter, so that the absorption near λ_0 make the greatest contribution to the index of refraction near λ_0, whereas the absorption values further from λ_0 make much smaller contributions. Data used in Eq. (3) covered the entire range over which significant changes in absorption were measured as a function of voltage (i.e., $\Delta\alpha \approx 0$ outside the data range). With knowledge of Δn and $\Delta\alpha_{abs}$ the large signal chirp is calculated as

$$\beta_c = \frac{4\pi}{\lambda}\frac{\Delta n}{\Delta\alpha_{abs}} \tag{4}$$

where it is understood that the change in absorption and index are a function of wavelength, bias voltage, and magnitude of voltage change. The absolute magnitude of absorption, as obtained in Eq. (1) is not necessary to accurately determine the chirp using Eq. (4); thus any wavelength and voltage independent errors in determining α have no effect on calculated β_c. In previous work [19], we have demonstrated that chirp predicted from photocurrent spectroscopy measurements agrees with measured chirp in devices fabricated from identical material.

3.2. Presentation of EAM characteristics

In order to compare the suitability of various materials for EAM device performance, one must simultaneously consider chirp parameter, insertion-loss, and extinction, as well as the wavelength range over which these parameters are satisfactory. Figs. 6–8 present large signal ($\Delta V = 2V$) chirp (β_c) as a function of bias (V_0) for four different wavelengths (λ_0) spanning a range of 30 nm. In Figs. 6–8, two separate low or negative chirp operating points are clearly marked for each wavelength (e.g., in Fig. 6, for each wavelength (λ_0), $\beta_c = 0.4$ and $\beta_c = 0.85$ operating points are marked with stars on the chirp (β_c) vs. voltage (V_0) line). The insertion-losses and extinction-ratios, in dB, at each of the marked operating points, are plotted against a secondary y-axis on the same graph. The extinction and

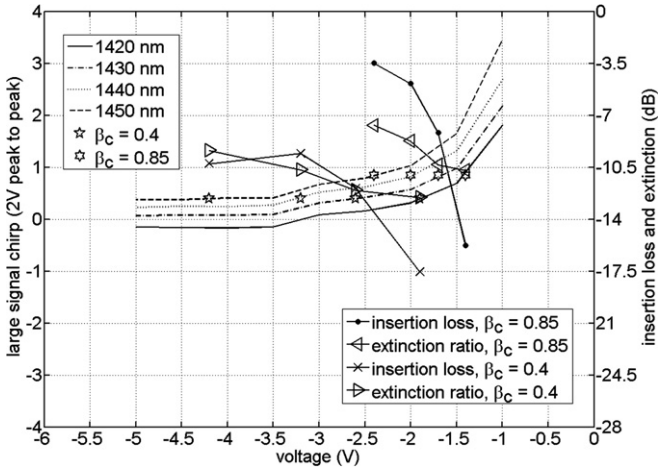

Fig. 6. Projected large signal chirp for a 125 μm modulator using 1.385Q bulk material having a 60% overlap with the optical mode. The lines curving downwards to the left are chirp as a function of voltage for four different wavelengths spanning 30 nm. Operating points for $\beta_c = 0.85$ and $\beta_c = 0.4$ are marked on each of these wavelength lines. Insertion-losses and extinction-ratios at these same operating points of $\beta_c = 0.85$ and $\beta_c = 0.4$ are also marked. Operation with negative chirp and acceptable insertion-loss and extinction is clearly not possible with this device.

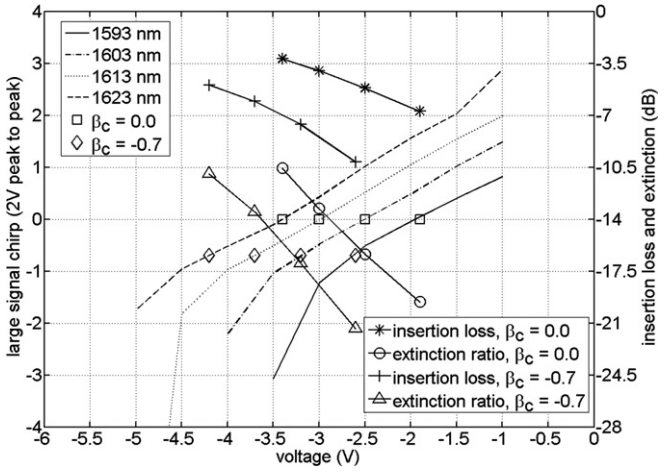

Fig. 7. Projected large signal chirp for a 125 μm modulator using 80 Å 85 meV wells having a 9% overlap with the optical mode. The lines curving downwards to the left are chirp as a function of voltage for four different wavelengths spanning 30 nm. Operating points for $\beta_c = 0.0$ and $\beta_c = -0.7$ are marked on each wavelength line. Insertion-losses and extinction-ratios at the $\beta_c = 0.0$ and $\beta_c = -0.7$ operating points are also marked. Clearly, negative chirp is readily available over a full 30 nm tuning range.

insertion-loss markers are connected by lines to highlight the trend in extinction and insertion-loss as a function of wavelength for a given chirp. With these graphs, one can simultaneously examine chirp, extinction, and insertion-loss as a function of wavelength and voltage. These novel figures simplify the evaluation of predicted EAM device performance.

Fig. 6 shows the predicted performance of the 1.385Q bulk material. Fig. 7 shows the predicted performance of the as-grown (i.e., not intermixed) 80 Å wells, and Fig. 8

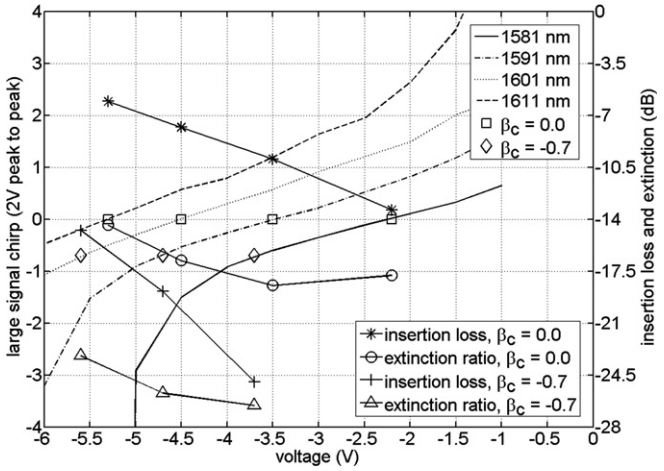

Fig. 8. Projected large signal chirp for a 125 μm modulator using 65 Å 120 meV wells having a 9% overlap with the optical mode. The lines curving downwards to the left are chirp as a function of voltage for four different wavelengths spanning 30 nm. Operating points for $\beta_c = 0.0$ and $\beta_c = -0.7$ are marked on each wavelength line. Insertion-loss and extinction-ratios at the $\beta_c = 0.0$ and $\beta_c = -0.7$ operating points are also marked. This device suffers from larger insertion-loss, smaller wavelength tuning range, and higher operating biases than the device in Fig. 7.

shows predicted performance for the as-grown 65 Å wells. The calculations for each of Figs. 6–8 assumed a modulator length of 125 μm. The confinement factor Γ was set at 9% for the QW structures, whereas Γ for the bulk material (Fig. 6) was set at 60%. These parameters reflect realistic values of actual devices, i.e., bulk materials have much larger overlaps [6] with the optical mode than QW material [27]. The overlap integral, Γ, scales the insertion-loss and extinction (Eq. (2)), but it does not affect the chirp parameter. Thus, for a given material, larger values of Γ will allow design of shorter EAMs. Shorter devices are preferable for high speed modulation in lumped element designs. Bulk material, however, has much lower absorption than QW material, so the higher value of Γ in bulk EAMs does not automatically allow shorter device length or higher extinction than in QW EAMs.

In each of Figs. 6–8, the detuning of the operating wavelengths from the modulator absorption-edge was chosen to allow maximum wavelength range with low or negative chirp. In Figs. 7 and 8, trends of insertion-loss and extinction as a function of wavelength clearly infer that moving to longer or shorter wavelengths will not improve performance. Longer wavelengths require much higher bias voltages, and shorter wavelengths introduce prohibitive insertion-loss. The wavelengths examined in Fig. 6 are unusually close to the modulator absorption-edge compared to bulk EAMs that are integrated with lasers using offset quantum-well technology [28]. The operating wavelengths in Fig. 6, do, however, highlight the difficulty of obtaining low chirp in a bulk device, regardless of integration platform (chirp is lower nearer the absorption-edge).

When interpreting Figs. 6–8, it is important to recall that for consistency and ease of comparison, all three sim-

Please cite this article in press as: Morrison GB et al., Electroabsorption modulator performance predicted ..., Solid State Electron (2006), doi:10.1016/j.sse.2006.10.013

ulated devices have lengths of 125 μm. Naturally, different epitaxy layer structures will be better suited to longer or shorter modulator lengths. Insertion-loss, for instance, can be greatly reduced by shortening the length of the device. Unfortunately, shortening the device also scales the extinction-ratio by the same amount as the insertion-loss. It is therefore important to consider the ratio between insertion-loss and extinction. Ideally, the insertion-loss should be much smaller than the extinction.

Figs. 6–8 compare values assuming a 2 V p–p drive signal. Depending on the application, larger or smaller drive signals could be used; the intent here is to demonstrate trends that offer insight into a broader spectrum of possible modulator designs and operating points.

The QW structures discussed in this paper were grown for use in integrated laser/EAMs, where the EAM portion is blue shifted by QWI. Thus the wavelengths considered for modulators fabricated from the as-grown wells are relatively long. Similar wells with the same characteristics could easily be grown for operation at shorter wavelengths. The effects of QWI on modulator performance are considered later in this paper.

3.3. Analysis and explanation of EAM performance

Comparison of Figs. 6–8 highlight the importance of choosing a suitable material structure when designing an EAM. The device fabricated from bulk material, shown in Fig. 6, exhibits relatively high (~10 dB) insertion-losses, even at a positive chirp of 0.4. The insertion-losses for $\beta_c = 0.4$ operating points in Fig. 6. are as large, or larger, than the available extinction-ratios, making operation at $\beta_c = 0.4$ difficult. At a chirp of $\beta_c = 0.85$, operation with extinction that is significantly larger than insertion-loss is possible, but only at the longer wavelengths. Operation at even longer wavelengths would decrease insertion-loss, but would increase chirp and decrease extinction (although the decreased extinction can be countered with greater modulator length). The wavelength range in Fig. 6 was chosen to demonstrate the futility of trying to obtain negative chirp in a simple bulk device. Larger extinction with lower insertion-loss is obtainable with bulk material in longer devices operated at wavelengths that are further from the modulator absorption-edge [6,28]. These longer devices suffer from large positive chirp parameters. Negative chirp with acceptable insertion-loss and extinction is unattainable with bulk material in a simple EAM. A relatively complex dual modulator configuration has been proposed to reduce chirp in bulk EAMs [29].

Fig. 7 demonstrates that an 80 Å QW structure will outperform bulk material. Chirp of 0 to −0.7 is available across a full 30 nm range, with much higher extinction-ratios and acceptable insertion-losses (<10 dB). Operating points for 0 to −0.7 chirp exhibit much larger extinction ratios than insertion-losses for the full 30 nm range. Excellent performance similar to that predicted in Fig. 7 has recently been reported in an EAM modulator designed using the same QWs [19].

Given that the 80 Å QWs of Figs. 4 and 7 are more suitable for EAM design than the bulk material of Figs. 3 and 6, one might assume that higher confinement and stronger excitons (i.e., more "quantum-well like" quantum wells) would lead to even better performance. Such an assumption is shown to be false in Fig. 8. The operating points in Fig. 8 have unacceptably high insertion-losses, especially for the $\beta_c = -0.7$ operating points. A shorter device would reduce insertion-loss, but would also reduce extinction. A reduced extinction is unacceptable because the ratios of insertion-loss to extinction in Fig. 8 are much less favorable than those in Fig. 7. In Fig. 8, much higher bias voltages, V_0, are required for low or negative chirp operation. As demonstrated by the wide spread of operation points relative to the x-axis, larger biases are also necessary to operate at longer wavelengths. Operation with −0.7 chirp is not possible at the longest (1611 nm) wavelength, even with a bias of −6 V. High voltages cause power inefficiency and heating and should be avoided.

Although modulator of Fig. 8 is difficult to operate at negative chirp, the 65 Å QW material from which it is fabricated exhibits a very pronounced exciton peak (Fig. 5). Thus, for applications tolerating positive chirp at a fixed wavelength, high extinction efficiencies in a relatively short device are feasible with large drive signals.

For the bulk material modulator of Fig. 6, increased voltages do not lower chirp beyond a certain bias point. In contrast, higher bias voltages, V_0, always result in lower, or more negative chirp for the QW materials of Figs. 7 and 8. The change in absorption-edge in these materials is actually a function of electric field rather than applied voltage. The electric field across the bulk material or quantum wells depends on the doping scheme in and around the waveguide. It is therefore highly desirable to design a structure that allows strong electric fields across the wells as a function of voltage, provided that the fields are less than breakdown strength. By increasing the available range of electric field in the wells, the bias voltage is reduced, and extinction efficiency is increased. Furthermore, negative chirp at longer wavelengths becomes attainable with more acceptable bias. In overly wide or shallow wells, however, high fields will destroy the exciton, and the structure will begin to exhibit less desirable properties similar to that of bulk material [30].

Our experimental results, which indicate that an 80 Å well has better negative chirp characteristics than a 65 Å well, are in keeping with purely theoretical calculations [31]. Slightly wider wells could further improve performance, but as demonstrated in Figs. 4 and 5, excitons are more easily quenched in wider wells, and in a well that is too wide the material properties will become bulk-like.

Deeper wells will have greater exciton strength, and might allow for shorter devices, but deeper wells are also more likely to suffer from saturation or poor RF perfor-

Please cite this article in press as: Morrison GB et al., Electroabsorption modulator performance predicted ..., Solid State Electron (2006), doi:10.1016/j.sse.2006.10.013

mance due to increased carrier escape times. The times for carrier escape by thermionic and tunneling mechanisms increase with increased well depth. Various mechanisms [5,32] have been proposed in order to maximize carrier sweep out time with minimal electric field, but such design considerations are beyond the scope of this paper.

The fact that negative chirp can be obtained in QW modulators, but not in bulk material modulators, stems from the presence of an exciton peak in the QW band-edge absorption spectra. The Kramers–Kronig integral (Eq. (3)) can be broken into a sum of two parts [31,33]: wavelengths longer than the operating wavelength (λ_0), and wavelengths shorter than the operating wavelength (λ_0). The part that is longer than the operating wavelength has a negative numerator and contributes negative values to the calculated change in index (ideal for negative chirp). The part that is at wavelengths shorter than the operating wavelength has a positive numerator, and contributes to positive index change (for positive absorption change). The numerator in the Kramers–Kronig transform of Eq. (3) also acts as a sampling window so that $\Delta\alpha$ near the wavelength in question make the most significant contributions to Δn. In bulk material, the large positive contribution from the short wavelength part of the Kramers–Kronig integral generally results in an overall net positive index change and hence a positive chirp, even in regions very close to the band-edge where insertion-loss is prohibitively high. In contrast, the QW band-edge absorption spectra have exciton peaks governed by the QCSE so that $\Delta\alpha_{abs}$ of Eq. (3) changes sign as a function of wavelength. This change in sign results in a short wavelength part of the Kramers–Kronig integral for Δn that is relatively small in magnitude compared to the negative, long wavelength part of the integral. Thus, with proper design, negative chirp is attainable with low insertion-loss, at lower voltages (V_0) [5], and over broad tuning ranges [34].

3.4. Quantum-well-intermixed material performance

The QWs discussed in this paper were also blue-shifted by QWI, as shown in Figs. 4 and 5. The QWI process is an ideal approach for monolithically integrated laser-EAM modulators [24,35]. The effect of QWI on modulator characteristics such as chirp, extinction, and insertion-loss, has not previously been investigated in depth. In Figs. 3 and 4, QWI reduces the magnitude of the exciton peak, and increases the decay of the exciton as a function of applied bias. It is therefore important to consider the effect that QWI will have on the performance of a QWI modulator.

In the case of both the 65 Å and 80 Å wells, the effect of QWI on modulator performance was detrimental, but in no way prohibitive. Figs. 9 and 10 show chirp, extinction, and insertion-loss for the 80 Å wells intermixed by 40 and 76 nm, respectively. The range of biases (V_0) necessary to obtain negative chirp across a 30 nm range do not significantly change in the QWI wells. Intermixing by an amount

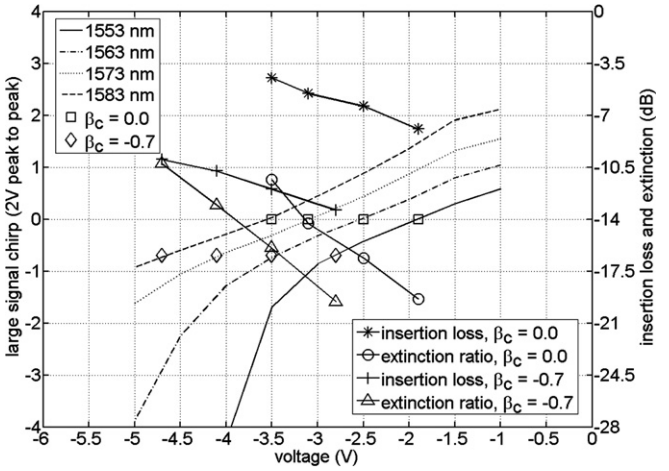

Fig. 9. Projected large signal chirp on a 2 V p–p signal for the 80 Å material after intermixing by 40 nm from 1548 nm to 1508 nm. The performance at 0 chirp is not significantly different from the as-grown material. Chirp of −0.7 is also available across the full range of wavelengths but the extinction vs insertion-loss ratio for $\beta_c = -0.7$ is not as favorable as it was for the as-grown material (Fig. 7).

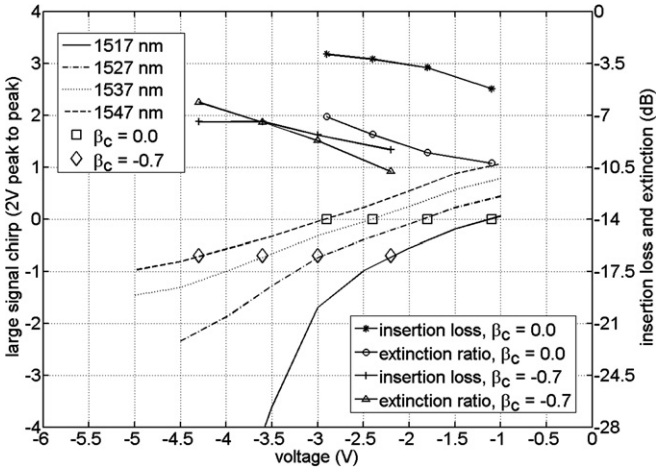

Fig. 10. Projected large signal chirp on a 2 V p–p signal for the 80 Å material after intermixing by 76 nm from 1548 nm to 1472 nm. The $\beta_c = -0.7$ ratio of extinction to insertion-loss is poor for the entire range of wavelengths, and both the extinction-ratio and insertion-loss have significantly decreased.

suitable for a modulator, e.g., 40 nm, results in no real change in expected modulator performance at 0 chirp. For $\beta_c = -0.7$, however, the insertion-loss increases noticeably, and the ratio of extinction to insertion-loss is less favorable, especially at longer wavelengths. Intermixing to the maximum extent possible (76 nm) results in very significant reduction of the exciton peak (Fig. 4) and as a result both the extinction and insertion-loss are significantly reduced. In the highly intermixed material, (Fig. 10) the $\beta_c = -0.7$ insertion-loss is approximately equal to the extinction-ratio across the entire range of wavelengths. This degradation in performance is due to the weakening of the exciton peak by the QWI process.

Please cite this article in press as: Morrison GB et al., Electroabsorption modulator performance predicted ..., Solid State Electron (2006), doi:10.1016/j.sse.2006.10.013

One possible method for improving the characteristics of the intermixed material would be to slightly increase the depth of the 80 Å wells. A deeper well would have better carrier confinement, and the intermixed material should then have an absorption-edge more similar to the as-grown material of Fig. 5.

4. Conclusion

The band-edge absorption spectra intrinsic to several different epitaxial layer structures have been collected by photocurrent spectroscopy. These band-edge absorption spectra have been used to predict the optimal conceivable performance of modulators fabricated from similar materials. Negative chirp appears unattainable in bulk EAMs that rely on the Franz–Keldysh effect. Negative chirp is attainable in QW structures, but 80 Å wells exhibit negative chirp over a wider tuning range and at lower biases than 65 Å wells, which is in keeping with theoretical predictions. The wider 80 Å wells were also shallower than the 65 Å wells, but the exciton peak was nonetheless resolvable at high biases, so that operation with negative chirp is attainable over a wide range (30 nm) of wavelengths. Wells that are much wider than 80 Å, or wells that are too shallow, will become increasingly ''bulk-like'', and will be poor candidates for EAM design. The optimum band-edge absorption spectra for an EAM modulator has maximum Stark shift with minimum exciton decay, thereby enabling high extinction as well as negative chirp over a wide tuning range. For optimal performance, the material should be incorporated into an EAM waveguide so as to maximize overlap with the optical mode and maximize the bias induced electric field.

QWI lowers carrier confinement and reduces the exciton peak, and therefore reduces modulator performance. The degree of quantum QWI necessary for optimal modulator absorption-edge placement, however, is small enough that the performance of QWI EAMs is acceptable. For QWI applications requiring passive material, the shallower 80 Å wells discussed in this paper may be less suitable than the 65 Å wells because the band-edge of the 85 Å wells cannot be blue-shifted as far as the narrower, deeper, 65 Å wells.

For fabrication of PICs in which passive waveguide regions are necessary, QWI has one significant advantage over other integration platforms. QWI PICs can be designed with EAMs having band-edges with relatively small blue-shifting from the lasing wavelength. The passive regions of the PIC can then be intermixed further [3] to minimize loss outside the modulator. In contrast, integration platforms that allow only two band-edges may need to compromise with EAM material that is detuned further from the lasing wavelength, thereby minimizing loss in ''passive'' waveguide regions. A modulator with larger detuning will, in general, result in higher biases, lower extinction, and larger chirp.

Acknowledgements

This work was supported in part by ARMY Grant DAAD19-03-1-0058. G.B. Morrison was supported in part by an NSERC Canada PDF.

References

[1] Studenkov PV, Xia F, Forest SR. Photonic integration using asymmetric twin-waveguide (atg) technology: Part II-Devices. IEEE J Sel Topics Quant Electron 2005;11(12):30–42.
[2] Studenkov PV, Xia F, Forest SR. Photonic integration using asymmetric twin-waveguide (ATG) technology: Part-I: concepts and theory. IEEE J Sel Topics Quant Electron 2005;11(1):15–29.
[3] Skogen EJ, Raring JW, Barton J, DenBaars S, Coldren LA. Post-growth control of the quantum-well band edge for the monolithic integration of widely-tunable lasers and electroabsorption modulators. IEEE J Sel Topics Quant Electron 2003;9(5):1183–90.
[4] Ramdane A, Krauz P, Rao EVK, Hamoudi A, Ougazzaden A, Robein D, et al. Monolithic integration of InGaAsP-InP strained layer distributed feedback laser and external modulator by selective quantum-well interdiffusion. IEEE Photon Technol Lett 1995;7(9):1016–8.
[5] Delprat D, Ramdane A, Ougazzaden A, Nakajima H, Carré M. Integrated multiquantum well distributed feedback laser-electroabsorption modulator with a negative chirp for zero bias voltage. Electron Lett 1997;33(1):853–5.
[6] Sysak MN, Barton JS, Johansson LA, Raring JW, Skogen EJ, Mašanović ML, et al. Single-chip wavelength conversion using a photocurrent-driven EAM integrated with a widely tunable sampled-grating DBR laser. IEEE Photon Technol Lett 2004;16(9):2093–5.
[7] Steinmann P, Borchert B, Stegmüller B. Improved behavior of monolithically integrated laser/modulator by modified identical active layer structure. IEEE Photon Technol Lett 1997;9(12):1561–3.
[8] Sysak MN, Barton JS, Raring JW, Dummer M, Tauke-Pedretti A, Blumenthal DJ, et al. 10 Gb/s photocurrent driven, widely tunable electroabsorption based wavelength converter. In: Optical fiber communication conference and exposition. Anaheim, CA, 2005, OtuM4.
[9] Nam ES, Lee SW, Jang DH, Lee JG, Pyun KE. Monolithis integration of a 1.55-μm strained multiple-quantum-well distributed feedback laser and quantum-confined stark-effect modulator by metal organic vapor-phase epitaxy using an InP-buffer-layer incorporated butt coupling scheme. J Korean Phys Soc 2000;36(4):228–32.
[10] Takeuchi H, Tsuzuki K, Sato K, Yamamoto M, Itaya Y, Sano A, et al. Very high-speed light-source module up to 40 Gb/s containing an MQW electroabsorption modulator integrated with a DFB laser. IEEE J Sel Topics Quant Electron 1997;3(3):336–43.
[11] Aoki M, Suzuki M, Sano H, Kawano T, Ido T, Taniwatari T, et al. InGaAs/InGaAsP MQW electroabsorption modulator integrated with a DFB laser fabricated by band-gap energy control selective area MOCVD. IEEE J Quantum Electron 1993;29(6):2088–96.
[12] Coldren LA, Corzine SW. Diode lasers and photonic integrated circuits. New York: John Wiley and Sons; 1995, p. 355–9.
[13] Alping A, Coldren LA. Electrorefraction in GaAs and InGaAsP and its application to phase modulators. J Appl Phys 1987;61(7):2430–3.
[14] Chuang SL. Physics of optoelectronic devices. New York: John Wiley and Sons; 1995, p. 557–72.
[15] Moseley AJ, Robbins DJ, Marshall AC, Kearley MQ, Davies JI. Quantum confined Stark effect in InGaAs/InP single quantum wells investigated by photocurrent spectroscopy. Semicond Sci Technol 1989;4(3):184–90.
[16] Wood TH. Direct measurement of the electric-field-dependent absorption coefficient in GaAs/AlGaAs multiple quantum wells. Appl Phys Lett 1986;48(21):1413–5.

[17] Charbonneau S, Koteles ES, Poole PJ, He JJ, Aers GC, Haysom J, et al. Photonic integrated circuits fabricated using ion implantation. IEEE J Sel Topics Quantum Electron 1998;4(4):772–93.
[18] Morrison GB, Skogen EJ, Wang CS, Raring JW, Chang Y, Sysak MN, et al. Photocurrent spectroscopy for quantum well intermixed photonic integrated circuit design. IEEE Photon Technol Lett 2005; 17(7):1414–6.
[19] Morrison GB, Raring JW, Skogen EJ, Wang CS, Coldren LA. Photocurrent spectroscopy analysis of widely tunable negative-chirp quantum-well intermixed laser-modulator transmitters. Appl Phys Lett 2005;86(71118):1–3.
[20] Kim I, Jang DH. Electroabsorption spectroscopy analysis of quantum-well modulator extinction and chirp. IEEE Photon Technol Lett 2004;6(11):2463–5.
[21] Gokhale MR, Studenkov PV, Ueng-McHale J, Thomson J, Yao J, van Saders J. Uncooled, 10 Gb/s 1310 nm electroabsorption modulated laser. In: Optical fiber communication conference 2003, PD-42.
[22] Raring JW, Skogen EJ, Johansson LA, Sysak MN, DenBaars SP, Coldren LA. Widely tunable negative-chirp SG-DBR laser/EA-modulated transmitter. IEEE J Lightwave Technol 2005;23(1):80–6.
[23] Miller DAB, Chemla DS, Damen TC, Gossard AC, Wiegmann W, Wood TH, et al. Electric field dependence of optical absorption near the band gap of quantum-well structures. Phys Rev B 1985;32(2): 1043–60.
[24] Skogen EJ, Raring JW, Morrison GB, Wang CS, Lal V, Masanovic ML, et al. Monolithically integrated active components: a quantum-well intermixing approach. IEEE J Sel Topics Quant Electron 2005;11(2):343–55.
[25] Agrawal GP. Fiber-optic communications systems. New York: John Wiley and Sons; 1997, p. 425–431.
[26] Henry CH, Logan RA, Bertness KA. Spectral dependence of the change in refractive index due to carrier injection in GaAs lasers. J Appl Phys 1981;52(7):4457–61.
[27] Skogen EJ, Wang CS, Raring JW, Morrison GB, Coldren LA. Small footprint, high-efficiency, integrated transmitters for high-speed optical interconnect applications. Integrated photonics research, San Francisco 2004, ITHD2.
[28] Mason B, Fish GA, DenBaars SP, Coldren LA. Widely tunable sampled grating DBR laser with integrated electroabsorption modulator. IEEE Photon Technol Lett 1999;11(6):638–40.
[29] Johansson LA, Akulova YA, Fish GA, Coldren LA. Sampled-grating DBR laser integrated with SOA and tandem electroabsorption modulator for chirp-control. IEE Electon Lett 2004;40(1):70–1.
[30] Miller DAB, Chemla DS, Schmitt-Rink S. Relation between electroabsorption in bulk semiconductors and in quantum wells: the quantum-confined Franz–Keldysh effect. Phys Rev B 1986;33(10): 6976–82.
[31] Yamanaka T, Wakita K, Yokoyama K. Potential chirp-free characteristics (negative chirp parameter) in electroabsorption modulation using a wide tensile strained quantum well structure. Appl Phys Lett 1996;68(22):3114–6.
[32] Sahara R, Morito K, Sato K, Kotaki Y, Soda H, Okazaki N. Strongly improved frequency response at high-optical input powers from InGaAsP compensated strain MQW electroabsorption modulators. IEEE Photon Technol Lett 1995;7(9):1004–6.
[33] Matsuda M, Morito K, Yamaji K, Fujii T, Kotaki Y. A novel method for designing chirp characteristics in electroabsorption MQW optical modulators. IEEE Photon Technol Lett 1998;10(3):364–6.
[34] Raring JW, Skogen EJ, DenBaars SP, Coldren LA. Demonstration of negative chirp characteristics over wide wavelength range using monolithically integrated SG-DBR laser/electroabsorption modulator. IEE Electron Lett 2004;40(25):1599–600.
[35] Qiu BC, Liu XF, Ke ML, Lee HK, Bryce AC, Aitchinson JS, et al. Monolithic fabrication of 2×2 crosspoint switches in InGaas-InAlGaAs multiple quantum wells using quantum well intermixing. IEEE Photon Technol Lett 2001;13(12):1292–4.

Please cite this article in press as: Morrison GB et al., Electroabsorption modulator performance predicted ..., Solid State Electron (2006), doi:10.1016/j.sse.2006.10.013